Nuclear Instruments and Methods in Physics Research A 383 (1996) 309–317

ELSEVIER

NUCLEAR INSTRUMENTS & METHODS IN PHYSICS RESEARCH Section A

Picosecond timing of terawatt laser pulses with the SLAC 46 GeV electron beam

T. Kotseroglou[a], C. Bamber[a], S. Boege[a], A.C. Melissinos[a,*], D.D. Meyerhofer[b], W. Ragg[a], C. Bula[c], K.T. McDonald[c], E.J. Prebys[c], D. Bernstein[d], D. Burke[d], E. Cisneros[d], R.C. Field[d], G. Horton-Smith[d], K. Jobe[d], J. Judkins[d], A.C. Odian[d], M. Ross[d], D. Waltz[d], S.C. Berridge[e], W.M. Bugg[e], K. Shmakov[e], A.W. Weidemann[e]

[a]*Department of Physics and Astronomy, University of Rochester, Rochester, NY 14627, USA*
[b]*Department of Mechanical Engineering, University of Rochester, Rochester, NY 14627, USA*
[c]*Joseph Henry Laboratories, Princeton University, Princeton, NJ, 08544, USA*
[d]*Stanford Linear Accelerator Center, Stanford University, Stanford, CA 94309, USA*
[e]*Department of Physics and Astronomy, University of Tennessee, Knoxville, TN 37996, USA*

Received 4 March 1996

Abstract

We report on the collision of 1.5 ps (FWHM) laser pulses traversing at 17° a short ~7 ps (FWHM) 46.6 GeV electron bunch. The phase-locked system used to maintain the correct timing of the laser pulses and the appropriate diagnostics are described. The jitter between the laser and electron pulses is determined from the stability of the observed rate of Compton scatters and can be described by a Gaussian distribution with $\sigma_j \simeq 2.2$ ps.

1. Introduction

In an experiment at the Stanford Linear Accelerator Center we are investigating the interaction of high energy electrons with the "critical field" of QED [1]. These conditions are achieved by scattering 46.6 GeV electrons from the focus of a short laser pulse with intensity in excess of 10^{18} W/cm^2 [2]. The root-mean-square (rms) electric field at the laser focus is $E_{\rm rms} = \sqrt{Z_0 I}$ (V/cm) where $Z_0 = 377\ \Omega$ is the impedance of free space and I is the laser intensity in W/cm^2. The field seen by a high energy electron in its own rest frame, as it crosses through the laser focus at an angle θ, is

$$E^* = (1 + \cos\theta)\gamma E_{\rm LAB}\,, \qquad (1)$$

where $\gamma = \varepsilon/m$ is the ratio of the electron energy to its rest-mass. For $I = 10^{18}$ W/cm^2 and $\varepsilon = 46.6$ GeV, $E^*_{\rm rms} = 3.5 \times 10^{15}$ V/cm as compared to the critical field value $E_c = m^2c^3/(e\hbar) = 1.3 \times 10^{16}$ V/cm.

At such field strengths, multiphoton Compton scattering and e^+e^- pair creation have significant probability and these processes are observed in the course of the experiment [3]. The experiment is located in the Final Focus Test Beam (FFTB) [4] because the low emittance and short pulse length of the FFTB are well matched to the focal dimensions of the laser pulse. A schematic of the interaction region and detector arrangement is given in Fig. 1. The laser pulse is focussed near its diffraction limit using $f/D = 6$ optics at the interaction point (IP). The laser pulse crosses the electron beam at an angle of 17° in the horizontal plane, as shown in more detail in Fig. 2.

Following the IP a string of six permanent magnets directs the electrons to the dump but also serves as an analyzing spectrometer for the electrons that scattered in the laser focus and for positrons produced in the collisions of the high-energy gammas with laser photons. The forward-going high-energy γ-rays are detected by a Cherenkov monitor; at the laser intensities achieved, 25% of the electrons that cross the focus interact. The scattered electrons, are detected in a moveable silicon–tungsten caloimeter, whereas positrons are detected by a separate calorimeter as shown in Fig. 1. Typically the Linac delivered pulses of 6×10^9 e^-; while the electron beam operated at 10 Hz, collisions occurred at a rate of 0.5 Hz because of the operating characteristics of the laser. Under optimal conditions laser pulses of energy $U = 1$ J were achieved in the green ($\lambda = 527$ nm) with FWHM = 1.2 ps and focussed to an area $A = 30\ \mu$m^2 [2].

For the electron pulse to cross through the laser focus the beams must be properly aligned in space and also properly timed. The transverse dimensions of the electron

* Corresponding author. Fax: +1 716 275 8527.

PII S0168-9002(96)00828-5

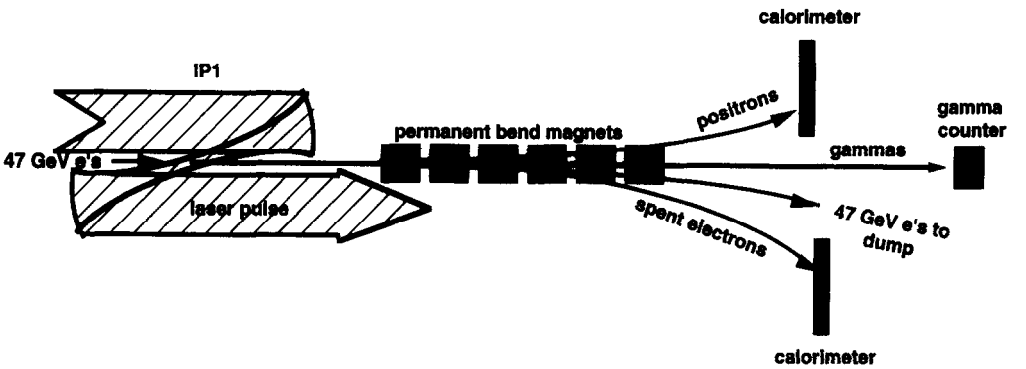

Fig. 1. Schematic representation of the laser–electron interaction region and of the detection apparatus.

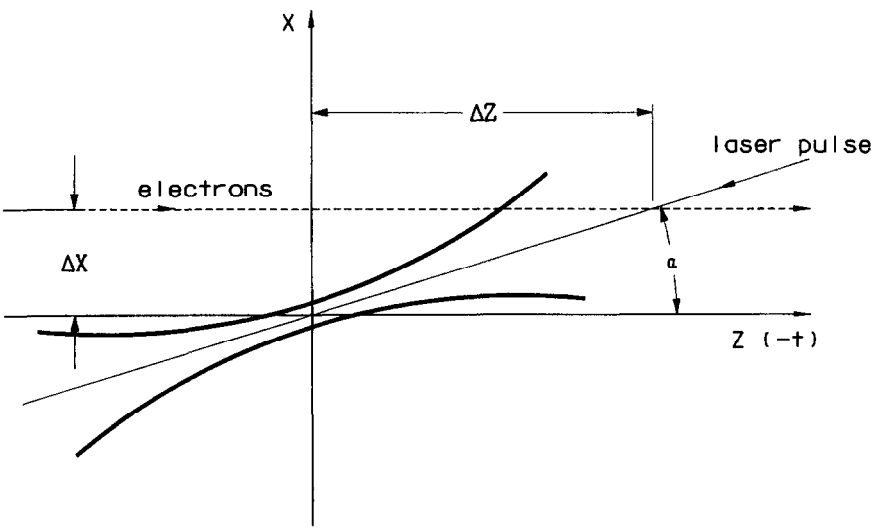

Fig. 2. The crossing geometry for the laser pulse and electron beam.

beam ($\sigma_x \sim \sigma_y \sim 40\ \mu m$) are significantly larger than the laser focal spot, so that collisions can be maintained during a "run" in spite of small drifts (of order 5 μm) in the electron beam position at the IP. To maintain the two signals at the correct timing, the laser oscillator is phase-locked to the linac radio frequency as discussed below. A particular pulse is selected from the oscillator pulse train, amplified and then transported to the IP along a 10 m long evacuated path. The overlap of the laser pulse with the electron bunch is adjusted by an optical delay line consisting of a prism mounted on a precision translation stage. The rate of laser-electron interactions as a function of relative delay between the two signals is shown in Fig. 3; it is fitted with a Gaussian yielding $\sigma_t = 3.4$ ps.

For head-on collisions the two beams would transverse through each other in a time interval $\Delta t \sim (\Delta z_l + \Delta z_e)/2c$

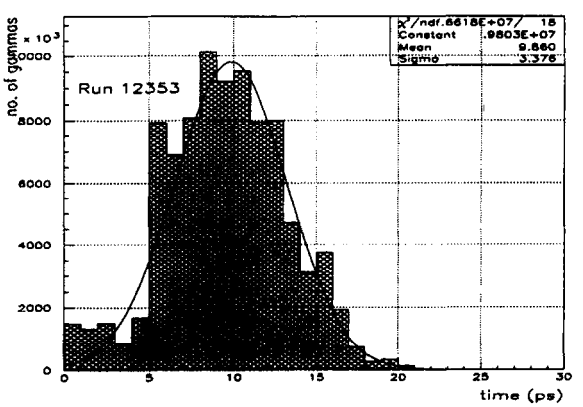

Fig. 3. A timing scan. The number of forward γ's is plotted as a function of delay of the optical pulse.

where Δz_l, Δz_e are the typical longitudinal dimensions of the laser focus and of the electron beam respectively. The FWHM for the electron beam was ~7 ps [5] and for the laser 1.2 ps; thus one expects that the overlap curve would have FWHM ~4.1 ps, or if it can be approximated by a Gaussian, $\sigma \simeq 1.7$ ps. However the overlap curve is broadened to twice this value by the finite transverse width of the electron beam (see Fig. 2) and by timing jitter.

2. The timing system

An overall schematic of the timing system is shown in Fig. 4. The master oscillator of the linac operates at $f_0 = 476$ MHz and is multiplied by 6 to drive the klystrons at 2856 MHz. The 476 MHz signal is transported from sector 30 – the end of the linac – to the laser room by a 600 m, low attenuation, temperature stabilized optical fiber [6]. The signal is then amplified and used to drive a Fiducial Output (FIDO) module which extracts the fiducial pulse, T_0, and produces the 4th subharmonic of the master frequency at 119 MHz. This signal is sent to a timing stabilizer module [7] which delivers 59.5 MHz; after amplification to 4 W the output of the stabilizer at 59.5 MHz drives the low-Q acousto-optic mode locker [8], in the ND:YLF laser oscillator cavity. A schematic of the laser system is shown in Fig. 5. The laser oscillator produces a pulse train at 119 MHz consisting of 60 ps long pulses. The pulses are chirped in a fiber and expanded in a grating pair before a single pulse is injected into the regenerative amplifier. For diagnostic purposes, a beam splitter sends a fraction of the pulse train to a pair of compression gratings, as well as to a photodiode. The photodiode signal is phase-compared in the timing stabilizer to the input radio frequency and locks the pulse train to the radio frequency. This feedback loop is shown in Fig. 6.

The laser triggering is based on the software-defined triggers of the Stanford Linear Collider (SLC) which are also synchronized with the master oscillator of the accelerator. These triggers can be tuned in both repetition rate and delay from a starting time T_0, which coincides with the injection of the electron beam. The laser trigger starts as a 10 Hz trigger and its delay is adjusted with a pulse delay unit (PDU), interfaced with the SLAC control program. The finest timing step of a PDU is 8 ns.

The PDU signal is frequency divided to 0.5 Hz, split and then fed into two commercial delay units [9] that can be timed in picosecond steps. One of them is used to trigger the lamps of the laser amplifiers and is irrelevant for

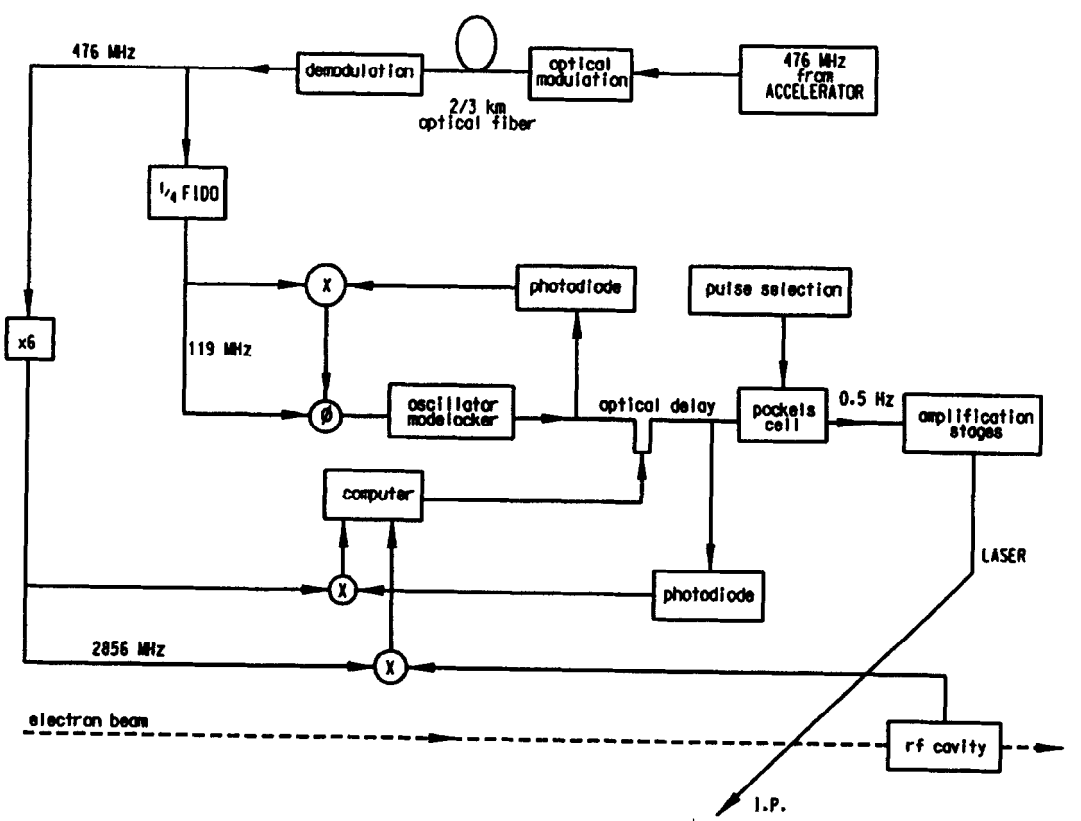

Fig. 4. Overview of the timing system for the synchronization of the laser pulses with the electron beam.

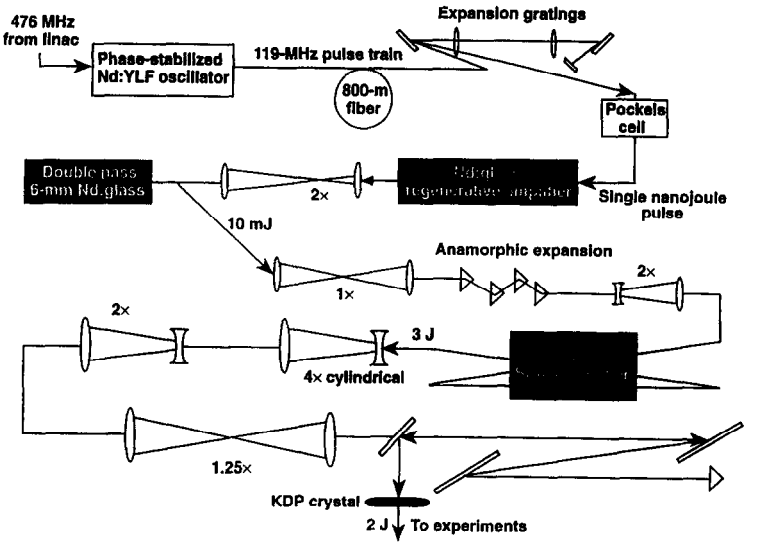

Fig. 5. Overall schematic of the laser system.

timing purposes since the lamp flash lasts for approximately 200 μs. The other delay unit triggers the 3 Pockels cells of the laser system. The last Pockels cell in the path of the laser defines the switchout time of the regenerative amplifier pulse train and thus selects the laser pulse that will collide with the electron beam. The timing of the other two Pockels cells is then adjusted relative to the switchout Pockels cell in order to achieve good amplification in the regenerative amplifier and good single-pulse contrast.

After the regenerative amplifier the laser pulse propagates through the rest of the laser chain and finally enters the input periscope in order to travel to the IP through the optical transport line. The leakage of the laser pulse from the first mirror of the periscope is detected in a photodiode, which is permanently positioned behind the mirror. The signal from this diode is the timing reference laser pulse and is compared with a signal derived from the electron beam.

The electron-beam signal is provided by a "ringing cavity" installed in the electron beam line, 60 cm downstream of the interaction point; the cavity has a resonant mode at 2856 MHz and quality factor $Q = 1300$. The cables from the ringing cavity and the photodiode patch cables are measured using "time delay reflectometry", while the optical transport length is determined by sending the laser pulse into the IP and measuring the relative delay of the input and return signals; this is achieved with two photodiodes. The signal from the laser diode is compared in a 400 MHz oscilloscope with the cavity signal. Thus coarse timing between the laser and electron pulses is established by stepping the delay to the laser trigger in the PDU in 8 ns steps; furthermore the phase of the reference radio frequency before the timing stabilizer is adjusted by using a cable delay box with ns steps. At this level the timing can be set to ±0.5 ns.

The pulses from the laser oscillator enter the variable optical delay line which is used to set the fine timing between the laser pulse and the electron bunch. The timing is changed by positioning the stage with μm precision either manually or through an HPIB interface of the stage driver with a PC. Since the stage is 25 cm long it can cover the range of ±0.8 ns. The PC interfaced into the stage driver is part of the Data Acquisition system and controlled by the central computer. Thus we can perform a real time scan of the laser pulse timing by correlating the optical delay with the observed rate of laser–electron interactions (see Fig. 3).

3. Study of timing jitter and long term drift

Both timing jitter and long-term drift are manifest at the picosecond timing level required in this experiment. These effects were studied with various diagnostics and ultimately through their effect on the collision rate.

The timing jitter of a periodic signal of frequency ω_0 can be determined from the power spectrum of a high harmonic, $n\omega_0$. For high values of n the phase noise dominates and contributes to the power spectrum a term proportional to $n^2\omega_0^2$. This contribution is parameterized by $n^2\omega_0^2 S_J(\omega - n\omega_0)$ which represents the ratio of the spectral density (in a 1 Hz bandwidth) at the offset $(\omega - n\omega_0)$, to the total power in the peak [10]. Thus $S_J(\omega - n\omega_0)$ has dimensions of time-cubed and the timing jitter is directly given by an integral over the spectrum of S_J,

$$\sigma_J^2 = \frac{1}{\pi}\int_{\omega'_{\text{low}}}^{\omega'_{\text{high}}} S_J(\omega')\,\mathrm{d}\omega', \tag{2}$$

where we have set $\omega' = (\omega - n\omega_0)$. The lower limit must

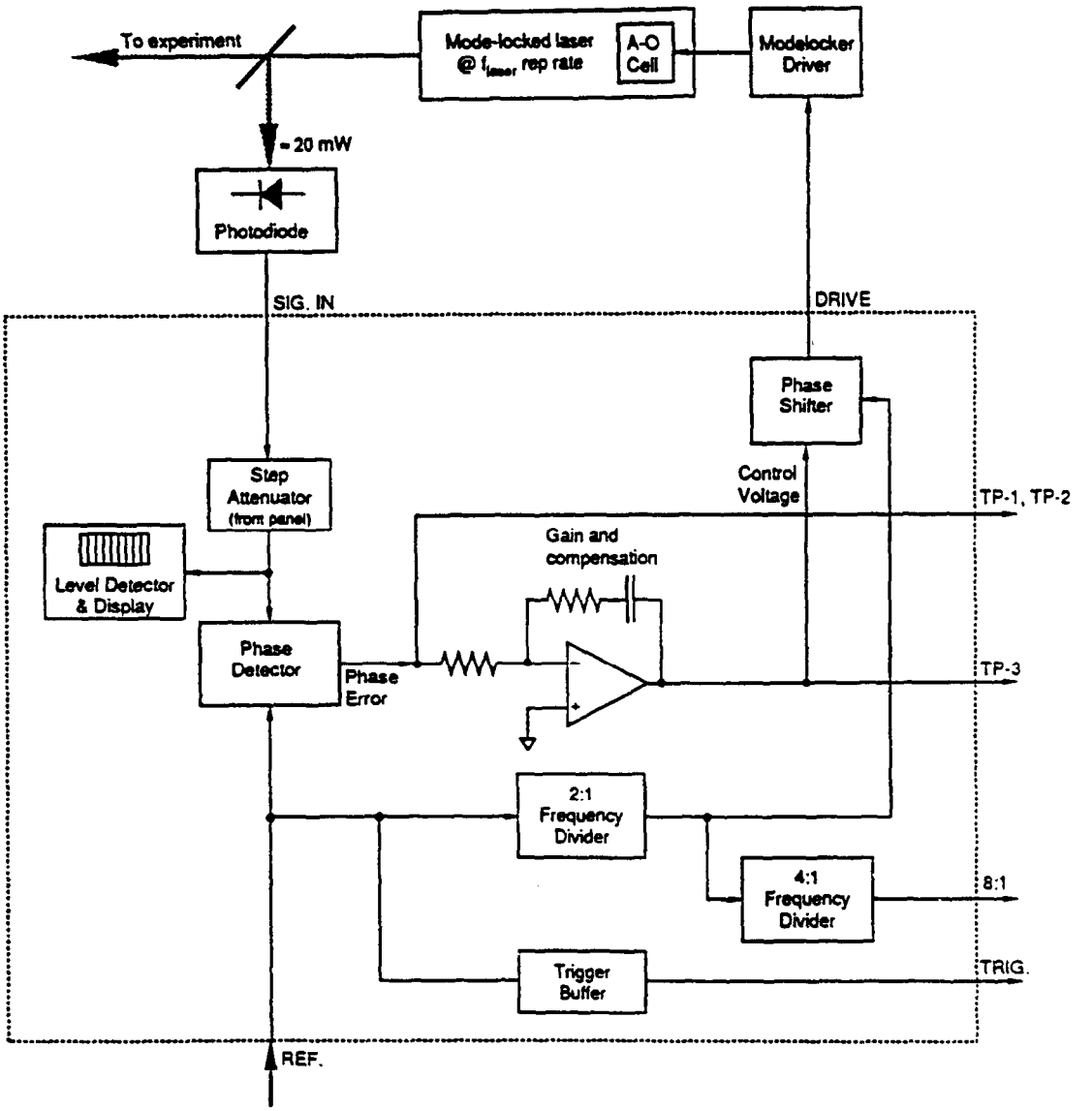

Fig. 6. The timing stabilizer (from Ref. [7]).

be chosen such that $\omega'_{low}\,\Delta T \sim 1$ where ΔT is the duration of the experiment, but often it is imposed by the resolution of the spectrum analyzer. An example of such a spectrum is shown in Fig. 7 for the fourth subharmonic of the 476 MHz signal after it has been transported by the optical fiber. For the laser we used a fast photodiode [11] to view the 24th harmonic of the pulse-trial and integrated $S_J(\omega')$ from $\omega'_{low} = 100$ Hz to $\omega'_{high} = 1.5$ kHz to find $\sigma_J \simeq 2.0$ ps.

Measurements can also be performed in the time domain by displaying the fast photodiode signal of the laser pulse train on a sampling oscilloscope [12]. The scope was triggered by the 119 MHz reference radio frequency. To reduce the effects of amplitude fluctuations we show in Fig. 8 the rising edge of the diode signal [peak amplitude 0.2 V, whereas the full scale of the display covers only 80 mV]. The distribution of the time of arrival is found to have $\sigma_{signal} = 4.3$ ps. However the jitter in the scope trigger was measured to have $\sigma_{scope} = 3.5$ ps indicating the limitations of the technique; nevertheless one is assured that the timing jitter of the laser pulse train had $\sigma_{laser} <$ 3 ps.

To measure long term drift (as contrasted to jitter) between the laser and electron signals we use a phase-comparison technique. It is advantageous to make the comparison at a high harmonic since then small time intervals correspond to larger phase shifts. The measurements reported here were made at 2856 MHz. The arrangement used to compare the laser pulse train to the reference

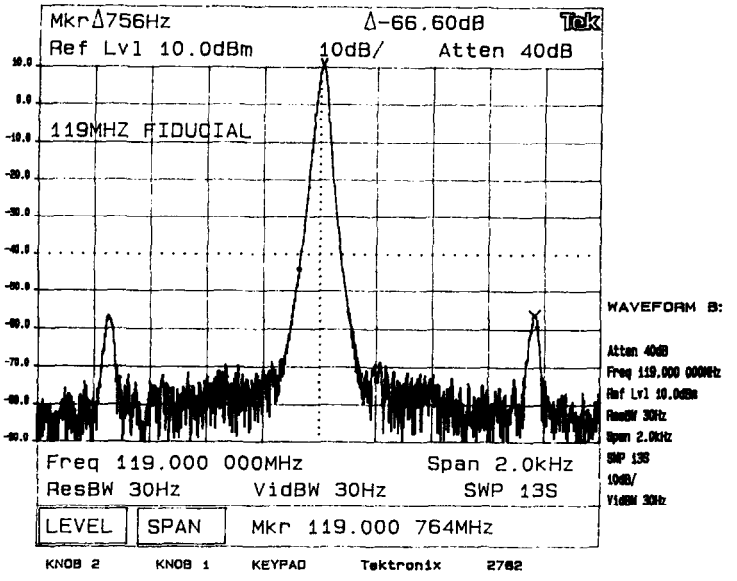

Fig. 7. Spectrum of the 4th subharmonic of the 476 MHz signal available in the laser room.

radio frequency is shown in Fig. 9. The 476 MHz output of the optical fiber is multiplied by six and fed to one arm of a double balanced mixer. The 24th harmonic of the laser pulse train detected by the diode is selected by a 2856 MHz Bessel filter, amplified by 60 dB, and then fed to the other arm of the mixer. The output of the mixer is filtered for DC with a lowpass 50 MHz filter and is sampled by an ADC card in one of the data acquisition PC's. Results are shown in Fig. 10 where the calibration corresponds to 1.9 mV/ps. With the timing stabilizer off large timing variations are observed, whereas with the stabilizer locked, the apparent fluctuations are at the 2.0 ps level.

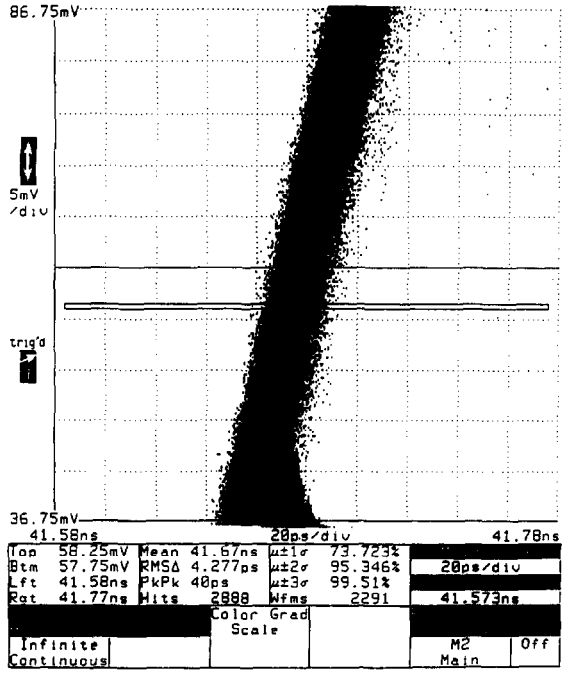

Fig. 8. Timing jitter measured in the time domain. The rising edge of the laser pulse train is shown with the sampling scope triggered by the reference radio frequency.

The stability of the electron beam with respect to the reference radio frequency is checked using the ringing cavity. The 2856 MHz signal from the cavity is transported to the laser room, amplified by 30 dB and phase-compared with the 476 MHz driving frequency (already multiplied by six). The system records a phase jitter measurement based on approximately 100 consecutive electron beam bunches and is interfaced with the linac control system. The rms jitter recorded by the cavity is about 0.3° at 2856 MHz, while when the electron beam is absent a pedestal rms noise of 0.1° is observed. Variations on a time scale of 30 min are less than 2 ps rms, while diurnal effects that change the length of the linac do change the electron timing on a timescale of hours. Fig. 11 shows the phase variation of the electron bunch with respect to the reference radio frequency in the laser room over 24 hours; also displayed are the "phase ramp" which is used by the accelerator operators to vary the phase of the electron beam manually and the barometric pressure. The strong correlation of the first two graphs shows that the radio frequency delivered to the laser room does not drift from the linac radio frequency. The correlation with the third graph is a consequence of the influence of atmospheric conditions on the effective length of the main drive line for the linac radio frequency.

Timing drift and jitter of the laser pulse arise from changes in the laser oscillator cavity length, thermal effects

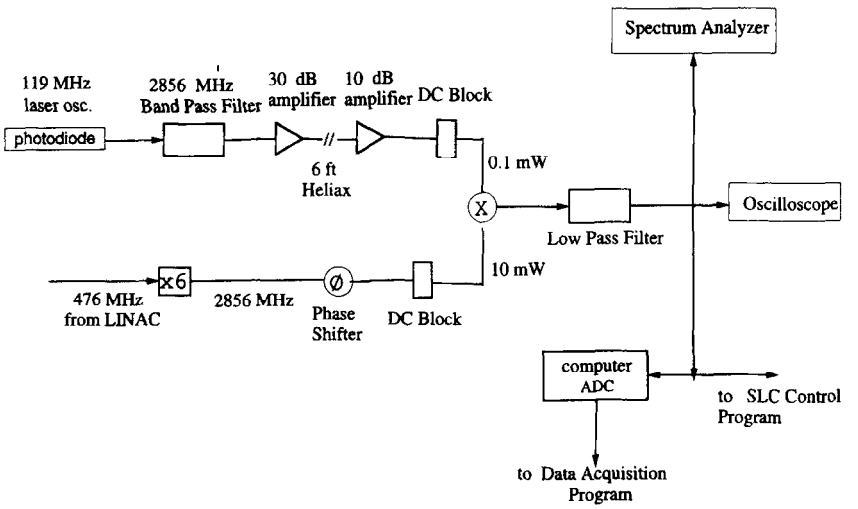

Fig. 9. Block diagram of the set-up used for phase comparison at 2856 MHz.

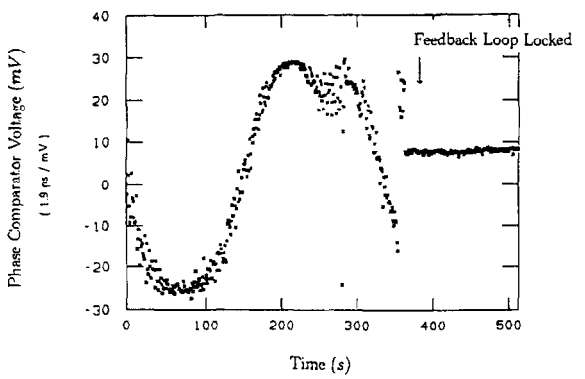

Fig. 10. Observed timing drift without and with the timing stabilizer locked.

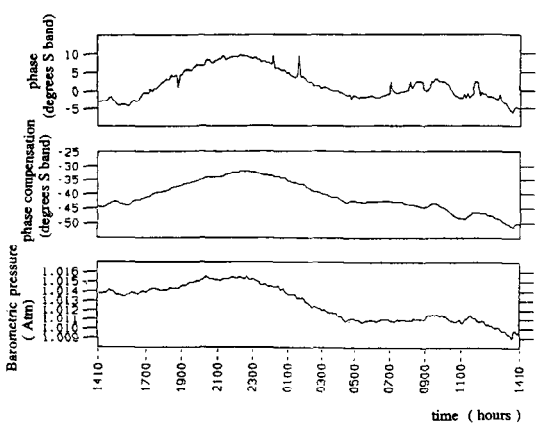

Fig. 11. (a) The electron beam phase drift with respect to the reference radio frequency signal, as measured by the ringing cavity, (b) changes in the "operators phase knob" and (c) ambient barometric pressure; all shown over a 24 hr period.

on the optics, turbulence in the cooling water flowing around the laser head and other mechanical vibrations. A discussion of these effects can be found in Ref. [13].

4. Conclusions from the observed collision rate

In the end, what is desired is a stable collision rate at maximum overlap of the laser pulse with the electron beam. Thus, the collision rate is the ultimate monitor of timing jitter after correction for other contributing factors such as beam current and size. A "timing curve" was shown in Fig. 3, where for a narrow electron beam and in the absence of jitter one would expect $\sigma = 1.7$ ps. The observed value is $\sigma = 3.4$ ps, and the contribution due to the transverse electron beam width is $\sigma_x/(\sin 17°) = 0.5$ ps, so that one estimates $\sigma_j \simeq [(3.4)^2 - (2.2)^2]^{1/2} = 2.6$ ps, consistent with previous estimates.

When observing ordinary Compton scattering the rate of high-energy γ's depends on the integral of the photon density over the path-length of the electrons through the laser beam; namely on the total number of photons (the energy) in the pulse. Therefore, and because the beams are crossing at an angle, the timing of the two pulses is correlated with the transverse displacement of the beam as can be seen in Fig. 2. We label the displacement of the beam from the position of the focus by Δx, and the difference from correct timing overlap by Δt. Then the rate of linear Compton Scattering does not change as long as

$$\frac{\Delta x}{\sin \alpha} = \frac{1}{2} c \, \Delta t \, . \tag{4}$$

This statement is valid for modest displacements such that the laser beam size does not exceed the vertical dimensions of the electron beam; in Eq. (4) α is the crossing angle in the horizontal plane, $\alpha = 17°$.

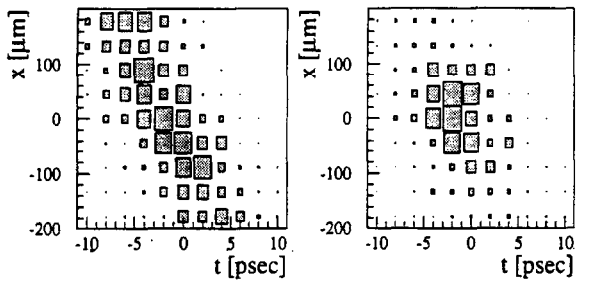

Fig. 12. (a) Linear Compton event rate as a function of transverse beam displacement and relative timing. (b) As above but for nonlinear events.

In contrast, nonlinear Compton scattering depends nonlinearly on the electric field strength, namely on a higher power of the photon density. Therefore the rate for nonlinear events is strongly dependent on whether the electrons cross the spatial location of the laser focus at the exact time at which the laser pulse reaches the focus. Figs. 12(a) and 12(b) show the results of an "x–t scan" where linear and nonlinear rates are plotted as a function of Δx and Δt on an 11×11 space-time grid, with 10 laser pulses at each point. In the linear case [Fig. 12(a)] the correlation predicted by Eq. (4) is clearly evident. In the nonlinear case [Fig. 12(b)] the profile of the focal spot is revealed, albeit with the resolution of the electron beam ($\sigma =$ 40 μm).

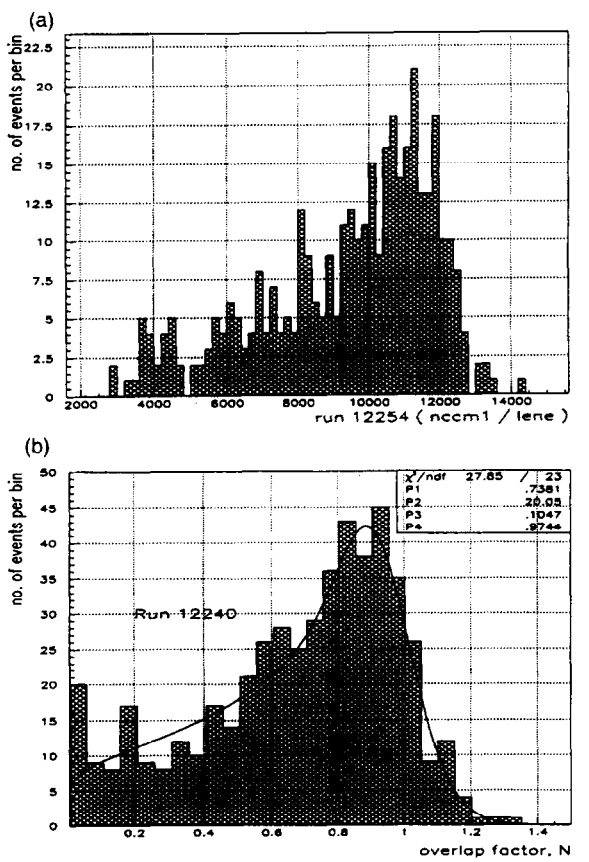

Fig. 13. Timing jitter estimate from the data runs. (a) The ratio of the number of gammas over the laser energy for a particular data run. (b) The "overlap factor" fitted as discussed in the text [Eq. (7)]; one finds $\sigma_0/\sigma_J = 0.98$.

A precise measure of the relative timing jitter can be obtained from the analysis of the data runs. Fig. 13(a) gives the distribution of the ratio of gammas detected divided by the laser energy, for a typical data run. In the absence of jitter and for constant electron beam parameters this ratio should have a fixed value, with a relatively small width corresponding to fluctuations arising from measurement errors. If the timing jitter is of the same order as the width of the temporal overlap of the two pulses (as measured by the timing curve of Fig. 3) the ratio will depart from its maximum tending to lower values; as the jitter increases, the peak is completely washed out. An equivalent representation (and which is to first order independent of variations in the electron beam parameter) is to plot the ratio of the number of gammas over the number of gammas predicted by the simulation for each event, taking into account not only the laser energy, but also the laser area and pulsewidth and the electron beam configuration for this event. This ratio should peak at one for perfect overlap conditions and will tend to zero for poor overlap. We call this ratio the "overlap factor", N and it is determined for each event as the ratio of the observed to the predicted yield. It is shown in Fig. 13(b) for a particular data run.

We obtain an expression for the probability distribution of the overlap factor N, as follows. If the time offset between the laser and electron beams is τ (τ is the difference from exact crossing) the overlap factor is given by

$$N(\tau) = \exp[-\tau^2/2\sigma_0^2], \tag{5}$$

where $\sigma_0^2 = \frac{1}{2}(\sigma_l^2 + \sigma_e^2)$ and σ_l, σ_e are the length of the laser and electron beams assumed to be Gaussian. The factor of $\frac{1}{2}$ is introduced because the two beams are counterpropagating. The time offset τ is taken to have a Gaussian probability distribution with mean zero and standard deviation σ_J, namely [14]

$$f(\tau) = \frac{1}{\sqrt{2\pi}} \frac{1}{\sigma_J} \exp[-\tau^2/2\sigma_J^2]. \tag{6}$$

To obtain the frequency function for N we note that $f(N)\,dN = f(\tau)\,d\tau$ so that

$$f(N) = \frac{1}{\sqrt{\pi}} \left(\frac{\sigma_0}{\sigma_J}\right) \frac{1}{N\sqrt{\ln(1/N)}} \exp[-\ln(1/N)(\sigma_0/\sigma_J)^2]$$

$$= \frac{R}{\sqrt{\pi}} \frac{N^{(R^2-1)}}{\sqrt{\ln(1/N)}}. \tag{7}$$

where we set $\sigma_0/\sigma_J = R$.

Eq. (7) was integrated over finite bins and smeared to account for the experimental resolution and then fit to the data of Fig. 13(b). The fit returns $R = \sigma_0/\sigma_j = 0.98 \pm 0.12$; therefore $\sigma_j \simeq \sigma_0 \simeq 2.2$ ps consistent with previous estimates, but with a small error (for this run $\sigma_e = 3$ ps, $\sigma_l = 0.64$ ps). Furthermore the $\chi^2 = 1.21$ per degree of freedom is supporting the assertion that the jitter is distributed as a Gaussian.

In conclusion we have shown that it is possible to maintain collisions between a 7-ps-long (FWHM) electron bunch and a 1.2-ps-long (FWHM) laser pulse. These techniques are important not only for studying nonlinear effects in high-energy electron scattering but also in the design of γ–γ colliders, laser X-ray sources and related applications. The timing jitter was found to be Gaussian distributed with a standard deviation $\sigma_j \simeq 2.2$ ps. This jitter was found to be Gaussian distributed with a standard deviation $\sigma_j \simeq 2.2$ ps. This jitter includes fluctuations both in the laser beam and in the electron beam.

Acknowledgements

We acknowledge with great appreciation the continued support of the SLAC staff and of the technical staff at our home Institutions. Mr. T. Blalock was instrumental in the construction of the laser system. This work was supported in part by Department of Energy grants DE-FG02-91ER40685, DE-FG02-91E40671, DE-FG05-91ER40627 and contract DE-AC03-76SF00515.

References

[1] The critical field is defined such that the energy gained by a singly charged particle in one electron Compton wavelength equals the electron rest-mass. Thus $E_c = m^2c^3/(e\hbar)$.

[2] C. Bamber et al., 0.5 Hz, phase-stabilized terawatt laser system with a Nd:glass slab amplifier for nonlinear QED experiments, University of Rochester preprint, UR-1428, (June 1995), submitted to Laser Phys.

[3] C. Bula et al., Phys. Rev. Lett. 76 (1996) 3116, see also C. Bula et al., Preliminary observation of nonlinear effects in Compton scattering presented at the 1995 Lepton–Photon Symp. Beijing, China.

[4] V. Balakin et al., Phys. Rev. Lett. 74 (1995) 2479.

[5] R.L. Holtzapple, Measurements of longitudinal phase space in the SLC LInac, SLAC-PUB-95-6841 (1995). Under optimal compression the pulse length of the SLC has $\sigma \sim$ 1.2 ps. In the experiment the longer pulse length was chosen to reduce the effects of timing jitter.

[6] Low thermal coefficient of delay time optical fiber cable, 6HJ-9336A, Sumitomo Electric Industries Ltd., Yokohama, Japan.

[7] Model 1000 Timing Stabilizer, Lightwave Electronics Co., Mountain View, CA, USA.

[8] Model ML-59.503B1 Acousto-optic mode locker, IntraAction Corp., Bellwood, IL, USA.

[9] Model DG535, Digital Delay/Pulse Generator, Stanford Research Systems, Sunnyvale, CA, USA.

[10] M.J.W. Rodwell, D.M. Bloom and K.J. Weingarten, IEEE J. Quantum Electronics 25 (1989) 817.

[11] Model No. HSDPS1, 20 GHz photodiode, Fermionics Corp., Simi Valley, CA, USA.

[12] Model CSA-803 Communications Signal Analyzer with an SD-24 TDR Sampling Head, Tektronix, Beaverton, OR, USA.

[13] Th. Kotseroglou, Observation of Nonlinear Compton Scattering, Ph.D. thesis, University of Rochester (1996) – UR1459.

[14] The probability of obtaining a value of τ between τ_1 and τ_2 is expressed in terms of the frequency function through $P(\tau_1 < \tau < \tau_2) = \int_{\tau_1}^{\tau_2} f(\tau)\,d\tau$.